Computation of Flowfields for Projectiles in Hypersonic Chemically Reacting Flows

Klaus A. Hoffmann*
Wichita State University, Wichita, Kansas 67208
Ting-Lung Chiang†
University of Texas at Austin, Austin, Texas 78712
and
Walter H. Rutledge‡
Sandia National Laboratories, Albuquerque, New Mexico 87185

A technique is presented for solving the inviscid, chemically reacting, hypersonic flowfield over axisymmetric blunt bodies. The Euler equations are solved using a fully implicit, flux vector splitting, finite-difference scheme. An approximate factorization scheme is also used in order to improve computational efficiency. Finite-rate chemical reaction calculations are decoupled from the gas dynamic equations in the current analysis. Complex blunt body shapes, including highly indented nose geometries, are analyzed for Mach numbers from 2 to 18.

Introduction

CURRENTLY there is a renewed interest in virtually all aspects of hypersonic aerodynamics. One particular area of interest is low-altitude, high-Mach conditions, which are important, for example, in the study of ballistic re-entry vehicles and electromagnetically accelerated kinetic energy projectiles. Flowfields created by such high-pressure, high-Reynolds number conditions pose an enormous aerodynamic heating and structural loading problem. These flowfields at hypersonic Mach numbers are almost always chemically reacting. Such chemical reactions can sometimes involve ionization in the shock layer, although they are normally dominated by dissociation and recombination of air molecules. Because of the high freestream density at low altitudes, such reacting flows are most likely in chemical equilibrium. For small projectiles, however, the effect of nonequilibrium chemistry may be important at altitudes as low as 25–30 km. Therefore, the inclusion of a nonequilibrium chemistry model is essential for accurate flowfield computations. Because of the extremely large Reynolds number conditions, the developing boundary layer over the blunt nose region of the hypersonic vehicle usually transitions from laminar to turbulent behavior near the stagnation point on the nosetip. Because of the high pressure and high temperature in the nose region, the turbulent boundary-layer heating rates are actually more severe than the "laminar" stagnation point heating. This increased heating phenomena has been demonstrated experimentally[1] and theoretically.[2] With increased heating rates downstream of the stagnation point, ablating thermal protection systems will experience larger surface recession rates aft of the actual nosetip. The resulting gouged surface creates an indented nose shape, which further aggravates the heating problem. These dynamic changes in body shape significantly alter the shock structure, pressure distribution, and pressure drag, as will be discussed in this paper.

Received March 22, 1989; revision received Jan. 31, 1990.

*Associate Professor, Department of Aerospace Engineering. Member AIAA.
†Research Engineer, Institute for Advanced Technology. Member AIAA.
‡Senior Member of Technical Staff. Senior Member AIAA.

There are several methods for calculating the pressure distribution over blunt bodies at hypersonic speeds. Many of these methods are simple approximations (such as modified Newtonian theory), and yet they yield satisfactory results for simple shapes.[3] The accuracy of some of these impact methods can be improved somewhat by the addition of nondimensional correlations between similarity parameters for pressure and geometry characteristics.[4] However, these simple surface inclination techniques can never predict the strong shock-shock interaction present with the current indented nose shapes and are best restricted to shapes with monotonically decreasing body slopes.

In order to predict accurately the surface properties along complex geometries, it is necessary that the analysis tool model the entire flowfield including the bow-shock shape and any embedded shock or expansion wave systems. These flowfield solvers involve the numerical solution of the full Navier-Stokes equations (Reynolds averaged) or some subset of these equations such as the Euler equations (i.e., inviscid flow), thin-layer Navier-Stokes equations, parabolized Navier-Stokes equations, etc. Because the major portion of the drag acting on an indented shape is wave drag, the current analysis will concentrate on the numerical solution of the Euler equations within a specified domain.

Numerous computational schemes for the solution of the Euler and Navier-Stokes equations have been investigated in the past. The formulations employing central-difference approximation of the convective terms usually require some type of artificial viscosity to damp out higher-order oscillations which occur in the vicinity of shock waves.[5,6] Recently, various upwind difference schemes[7–9] have gained popularity due to their robustness. In this current study, the Euler equations are solved by the flux-vector splitting scheme of Steger and Warming[10] for various indented nosetips. To increase the range of applicability and remove restrictions on projectile size due to chemistry considerations, a nonequilibrium chemistry model has been incorporated. To illustrate the mixed equilibrium/nonequilibrium region within a typical flowfield, the freestream condition corresponding to an altitude of 30 km was selected. The freestream pressure and temperature for this altitude were 1197 N/m^2 and 226.5 K, respectively.

Governing Equations

In order to determine the hypersonic inviscid flowfield about a complex geometry, a computational fluid dynamics

(CFD) scheme has been developed that solves the Euler equations within a fixed domain. Within this domain, all shock waves are numerically captured by casting the nondimensionalized governing equations, for an axisymmetric configuration, in conservation form, as

$$\frac{\partial Q}{\partial t}+\frac{\partial E}{\partial x}+\frac{\partial F}{\partial y}+H=0 \tag{1}$$

where

$$Q=\begin{bmatrix}\rho\\ \rho u\\ \rho v\\ \rho e_t\end{bmatrix} \quad E=\begin{bmatrix}\rho u\\ \rho u^2+p\\ \rho uv\\ (\rho e_t+p)u\end{bmatrix}$$

$$F=\begin{bmatrix}\rho v\\ \rho uv\\ \rho v^2+p\\ (\rho e_t+p)v\end{bmatrix} \quad H=\frac{1}{y}\begin{bmatrix}\rho v\\ \rho uv\\ \rho v^2\\ (\rho e_t+p)v\end{bmatrix}$$

These equations represent the conservation of mass, x component of the conservation of momentum, y component of the conservation of momentum, and the conservation of energy, respectively. The last term in Eq. (1), the H term, represents the source term in the y or axisymmetric direction and is the reason that Eq. (1) is sometimes referred to as the "weak conservation form."

A coordinate transformation, which converts the governing equations from axisymmetric coordinates (t,x,y) to a body-fitted coordinate system (τ,ξ,η) in which ξ is aligned with the local surface, is now introduced. This new coordinate system allows easier implementation of body-boundary conditions and finite-difference algorithms. In the computational space, grid points are evenly spaced such that $\Delta\xi$ and $\Delta\eta$ are both constant. The generalized transformation is obtained by specifying a curvilinear coordinate system that will map the nonrectangular physical grid system to a rectangular computational grid system. The resulting transformed governing equations are

$$\frac{\partial \bar{Q}}{\partial \tau}+\frac{\partial \bar{E}}{\partial \xi}+\frac{\partial \bar{F}}{\partial \eta}+\bar{H}=0 \tag{2}$$

where

$$\bar{Q}=\frac{Q}{J}$$

$$\bar{E}=\frac{1}{J}\left[\xi_t Q+\xi_x E+\xi_y F\right]$$

$$\bar{F}=\frac{1}{J}\left[\eta_t Q+\eta_x E+\eta_y F\right]$$

and

$$\bar{H}=\frac{H}{J}$$

Complete details of the generalized coordinate transformation are discussed in Ref. 11. The metrics of transformation are

$$\xi_x=Jy_\eta \qquad \eta_x=-Jy_\xi$$

$$\xi_y=-Jx_\eta \qquad \eta_y=Jx_\xi$$

and the Jacobian of transformation is defined by

$$J=\frac{1}{x_\xi y_\eta-y_\xi x_\eta}$$

This Jacobian of transformation and all of the metrics are determined numerically using a second-order, finite-difference scheme from the results of an elliptic grid generator.

Numerical Algorithm

A fully implicit scheme is used to obtain a set of finite-difference equations in the computational space (τ,ξ,η) based on Eq. (2). This finite-difference scheme involves a first-order, backward-differencing scheme in time and a subsequent linearization of the nonlinear spatial flux terms in Eq. (2). The flux terms $\bar{E}$, $\bar{F}$, and $\bar{H}$ are nonlinear in $\bar{Q}$ and can be approximated as

$$\bar{E}^{n+1}\cong\bar{E}^n+\frac{\partial\bar{E}}{\partial\bar{Q}}\Delta\bar{Q}+O(\Delta\tau^2)$$

$$\bar{F}^{n+1}\cong\bar{F}^n+\frac{\partial\bar{F}}{\partial\bar{Q}}\Delta\bar{Q}+O(\Delta\tau^2)$$

$$\bar{H}^{n+1}\cong\bar{H}^n+\frac{\partial\bar{H}}{\partial\bar{Q}}\Delta\bar{Q}+O(\Delta\tau^2)$$

Therefore, the transformed governing equations at time level $n+1$ are simply

$$\left[I+\Delta\tau\left(\frac{\partial A}{\partial\xi}+\frac{\partial B}{\partial\eta}+C\right)\right]\Delta\bar{Q}$$
$$=-\Delta\tau\left[\left(\frac{\partial\bar{E}}{\partial\xi}\right)^n+\left(\frac{\partial\bar{F}}{\partial\eta}\right)^n+(\bar{H})^n\right]$$

where

$$\Delta\bar{Q}=\bar{Q}^{n+1}-\bar{Q}^n$$

and the Jacobian matrices A, B, and C are defined as

$$A=\left(\frac{\partial\bar{E}}{\partial\bar{Q}}\right)^n$$

$$B=\left(\frac{\partial\bar{F}}{\partial\bar{Q}}\right)^n$$

$$C=\left(\frac{\partial\bar{H}}{\partial\bar{Q}}\right)^n$$

Finally, if a five-point spatial differencing scheme (e.g., central differencing) is used, then the result is a 4×4 block pentadiagonal system of equations. Therefore, in order to increase computational efficiency, an approximate factorization technique is introduced to convert the pentadiagonal system of equations into two sets of tridiagonal systems of equations. This procedure yields the following form of the governing equations:

$$\left[I+\Delta\tau\frac{\partial A}{\partial\xi}\right]\left[I+\Delta\tau\left(\frac{\partial B}{\partial\eta}+C\right)\right]\Delta\bar{Q}$$
$$=-\Delta\tau\left[\left(\frac{\partial\bar{E}}{\partial\xi}\right)^n+\left(\frac{\partial\bar{F}}{\partial\eta}\right)^n+(\bar{H})^n\right] \tag{3}$$

This equation is said to be in factored delta form since the unknown $\bar{Q}$ vector at time level $n+1$ is isolated in $\Delta\bar{Q}$. Actual implementation of Eq. (3) requires a two-step solution (i.e., alternating sweeps in η and ξ). This two-step process is illustrated below by finding an intermediate $\Delta\bar{Q}^*$ vector that is then applied to the second step:

$$\left[I+\Delta\tau\frac{\partial A}{\partial\xi}\right]\Delta\bar{Q}=-\Delta\tau\left[\left(\frac{\partial\bar{E}}{\partial\xi}\right)^n+\left(\frac{\partial\bar{F}}{\partial\eta}\right)^n+(\bar{H})^n\right]$$

followed by

$$\left[I + \Delta\tau\left(\frac{\partial B}{\partial \eta} + C\right)\right]\Delta\bar{Q} = \Delta\bar{Q}^*$$

Many authors use a five-point, central-differencing scheme such as the Beam and Warming[12] scheme for the convective or inertial terms. Unfortunately, such central-difference schemes introduce undesirable oscillations and require an "artificial viscosity" term for damping. Alternatively, the current investigation has utilized the Steger-Warming first-order flux vector splitting technique, which still only requires a five-point stencil. The flux vector splitting approach applies simple forward- and backward-differencing schemes without violating the zone of silence/dependence principle. In this procedure the flux vectors $\bar{E}$ and $\bar{F}$ and the flux vector Jacobians A and B are split along the respective eigenvalues of the Jacobian matrices. An algebraic manipulator program called MACSYMA[13] has been used to find these eigenvalues. The resulting eigenvalues of A are

$$\lambda\xi_1 = \xi_t + \xi_x u + \xi_y v$$

$$\lambda\xi_2 = \xi_t + \xi_x u + \xi_y v$$

$$\lambda\xi_3 = \xi_t + \xi_x u + \xi_y v + a\sqrt{\xi_x^2 + \xi_y^2}$$

$$\lambda\xi_4 = \xi_t + \xi_x u + \xi_y v - a\sqrt{\xi_x^2 + \xi_y^2}$$

The eigenvalues of B are similar to those of A. For the Jacobian B, substitute η for ξ at all points in the above equations. In the Steger-Warming scheme, first-order, backward differencing is used for positive eigenvalues and forward differencing for negative values. The resulting finite-difference equation with the approximate factorization two-sweep scheme is

$$\left(-\frac{\Delta\tau}{\Delta\xi}A^+_{i-1,j}\right)\Delta\bar{Q}^*_{i-1,j} + \left[I + \frac{\Delta\tau}{\Delta\xi}(A^+_{i,j} - A^-_{i,j})\right]\Delta\bar{Q}^*_{i,j} + \left(\frac{\Delta\tau}{\Delta\xi}A^-_{i+1,j}\right)\Delta\bar{Q}^*_{i+1,j} = -\Delta\tau\left[\frac{1}{\Delta\xi}(\bar{E}^+_{i,j} - \bar{E}^+_{i-1,j} + \bar{E}^-_{i+1,j} - \bar{E}^-_{i,j}) + \frac{1}{\Delta\eta}(\bar{F}^+_{i,j} - \bar{F}^+_{i,j-1} + \bar{F}^-_{i,j+1} - \bar{F}^-_{i,j}) + \bar{H}_{i,j}\right] \quad (4a)$$

and

$$\left(-\frac{\Delta\tau}{\Delta\eta}B^+_{i,j-1}\right)\Delta\bar{Q}_{i,j-1} + \left[I + \frac{\Delta\tau}{\Delta\eta}(B^+_{i,j} - B^-_{i,j}) + \Delta\tau C_{i,j}\right]\Delta\bar{Q}_{i,j} + \left(\frac{\Delta\tau}{\Delta\eta}B^-_{i,j+1}\right)\Delta\bar{Q}_{i,j+1} = \Delta\bar{Q}^*_{i,j} \quad (4b)$$

These equations represent two sets of block tridiagonal systems of equations.

As mentioned previously, the grid system for this study is generated using a standard elliptic grid generation scheme.[14] The actual elliptic partial differential equations to be solved for x and y are

$$ax_{\xi\xi} - 2bx_{\xi\eta} + cx_{\eta\eta} = -\frac{1}{J^2}(x_\xi P + x_\eta Q) \quad (5a)$$

$$ay_{\xi\xi} - 2by_{\xi\eta} + cy_{\eta\eta} = -\frac{1}{J^2}(y_\xi P + y_\eta Q) \quad (5b)$$

where

$$a = x_\eta^2 + y_\eta^2$$

$$b = x_\xi x_\eta + y_\xi y_\eta$$

and

$$c = x_\xi^2 + y_\xi^2$$

and P and Q are optionally prescribed control functions.

Chemical Model

At high Mach numbers, most of the freestream kinetic energy of the flow is converted into internal energy across a normal shock in the vicinity of the stagnation region. Because of the great amount of newly generated internal energy, not all of this energy can be absorbed into the thermal energy (i.e., temperature) of the air molecules (e.g., vibrational, rotational, etc.). Therefore, some of the internal energy goes into breaking the molecular bonds between the atoms resulting in molecular dissociation. If the freestream speeds were large enough, then part of the excess internal energy would also go into stripping off electrons from molecules and dissociated atoms (i.e., ionization). Obviously, at high speeds (e.g., $M_\infty > 6$) the assumption of a calorically perfect gas (i.e., ideal gas) is clearly invalid. In fact, for the larger Mach numbers over the range of current interest (i.e., 2–18), the assumption of thermally perfect gas is also in question. In order to predict accurately static temperature levels in the shock layer, some type of chemical model will have to be incorporated into the solution procedure. At lower altitudes the flowfield shifts toward chemical equilibrium implying that the chemical reactions rates are almost instantaneous. At higher altitudes, however, low density reduces the reactions to a finite rate, and the flowfield may be in chemical nonequilibrium.

In the current analysis, effects due to ionization will not be considered. However, possible dissociation and recombination will be modeled using a nonequilibrium chemistry model. Furthermore, the freestream air will be assumed to be a binary species combination of O_2 and N_2. The resulting reactions to be considered are

$$O_2 + M \rightleftharpoons 2O + M$$

$$N_2 + M \rightleftharpoons 2N + M$$

$$NO + M \rightleftharpoons N + O + M$$

$$NO + O \rightleftharpoons N + O_2$$

$$O + N_2 \rightleftharpoons N + NO$$

where M represents nonreacting heavy particles that may be any one of the five species, O_2, N_2, NO, O, and N. The choice of a nonequilibrium model vs an equilibrium model was made to accommodate future extensions to higher altitude applications.

However, it is emphasized that the nonequilibrium model can be used at the lower altitudes as well to compute equilibrium conditions. Therefore, for situations where some uncertainty as to the state of chemistry that exists, the choice of the nonequilibrium model is required.

The particular nonequilibrium model used in this study was that of Lee.[15] The governing equations are the species continuity equations written in computational space as

$$\frac{\partial}{\partial\tau}(\rho\bar{c}_s) + \frac{\partial}{\partial\xi}[\rho\bar{c}_s(u\xi_x + v\xi_y)] + \frac{\partial}{\partial\eta}[\rho\bar{c}_s(u\xi_x + v\xi_y)] + \frac{1}{y}(\rho v\bar{c}_s) = \bar{w}_s$$

where s represents each of five species and

$$\bar{c}_s = \frac{c_s}{J} \qquad \bar{w}_s = \frac{\dot{w}_s}{J}$$

In this equation c_s is the mass fraction of s, and $\dot{w}_s$ is the mass production rate per unit volume of s. Note that the global continuity equation is obtained by adding up each of the species equations. The rate equations and the rate data used in the study are given in Ref. 16. These species equations can be decoupled or coupled with the gas dynamic equations. In the current study, a decoupled procedure has been implemented to avoid the added difficulty with increasing the block tridiagonal solvers from a 4×4 block to an 8×8 block. Even though decoupled, the species equations are solved implicitly because of the stiffness associated with these equations, especially for chemical equilibrium conditions. The boundary conditions of the species equations are applied implicitly using the requirement of zero normal gradient at the surface.

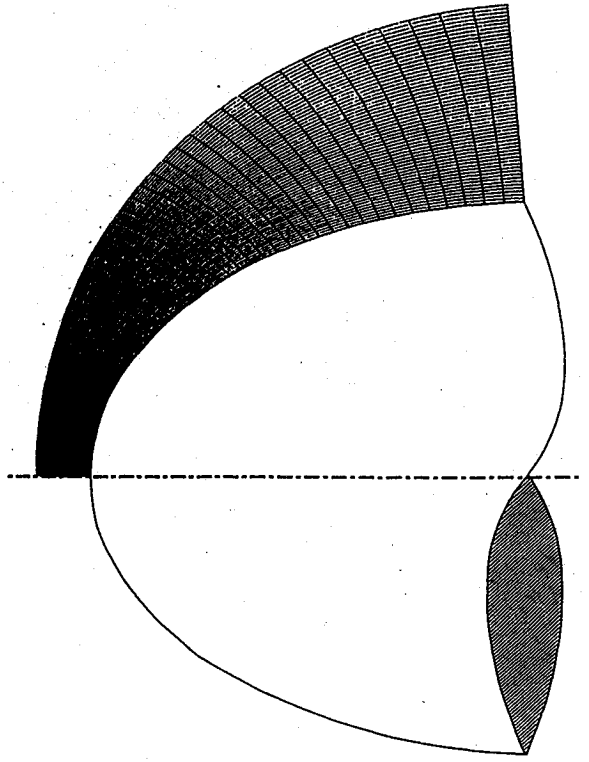

Fig. 1 Grid system for configuration 1.

Results

The severe aerothermodynamic environment experienced during hypersonic flight can cause enormous heating rates and subsequent surface recession for ablating nosetip geometries. Early boundary-layer transition at low altitudes can further aggravate the nose ablation phenomena and produce indented nose shapes. If recession and/or surface shape change is severe, then structural failure of the vehicle is possible or, at least, some degradation of vehicle performance is likely. In order to investigate these phenomena, the numerical procedure previously discussed was used to compute the inviscid flowfields for the nose regions of three configurations representing possible sequential degradation. For each of the three configurations, a 71×55 grid was used and produced by an elliptic grid generator. Even though the solution algorithm was based on an implicit formulation in time, a stability criterion was necessary for a successful computation. This restriction on $\Delta\tau$ is a result of the nonlinear nature of the governing differential equations. A Courant number of the form

$$\left|\lambda_{\max}\left|\frac{\Delta\tau}{\Delta\xi}\right.\right.$$

$$\left|\lambda_{\max}\left|\frac{\Delta\tau}{\Delta\eta}\right.\right.$$

was used to define the relations between the physical grid spacing and the time step. If the grid points in the stagnation region were clustered so that the Courant number did not exceed the specified value (usually 1), then satisfactory convergence was achieved. However, it is cautioned that the stability requirement due to chemistry must also be considered where the nonequilibrium effects are important. For low-altitude conditions where the nonequilibrium effect is included, the stability restriction of the chemistry equations can surpass those of the Courant number restriction of the Euler equations. A detailed stability analysis of this decoupled scheme can be found in Ref. 17.

Configuration 1 represents an initial unablated shape and is shown in Fig. 1 as an elliptically shaped body. Isobars of this configuration are presented for Mach numbers of 2, 12, and 18 in Figs. 2–4, respectively. These isobars illustrate contours of pressure nondimensionalized by $\rho_\infty U_\infty^2$. Note the similarity in Figs. 2–4 with the only significant difference being decreasing shock standoff distance and shock-layer thickness with increasing Mach number.

Configuration 2 represents a moderate amount of surface erosion due to a turbulent boundary layer on the nose at

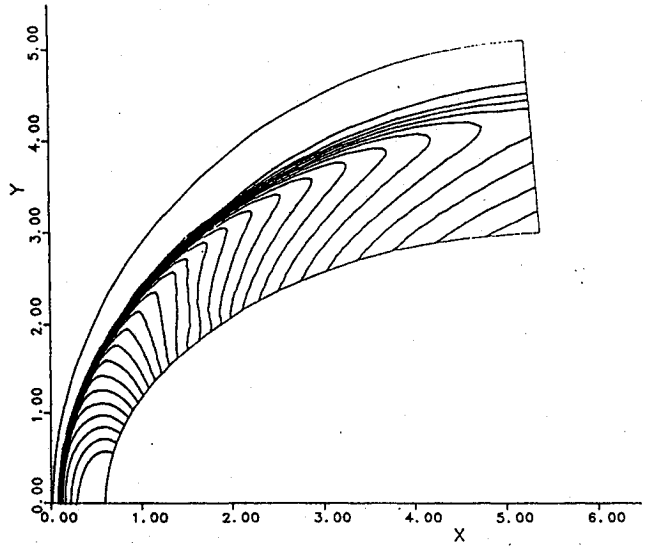

Fig. 2 Isobars for configuration 1 at freestream Mach number of 2.

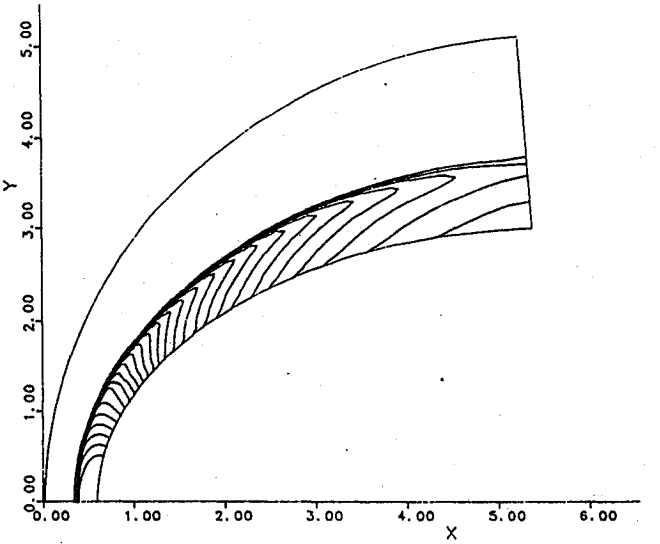

Fig. 3 Isobars for configuration 1 at freestream Mach number of 12.

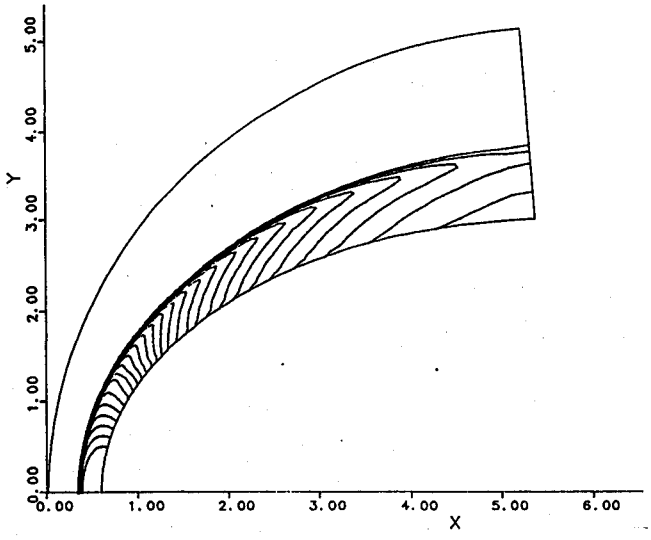

Fig. 4 Isobars for configuration 1 at freestream Mach number of 18.

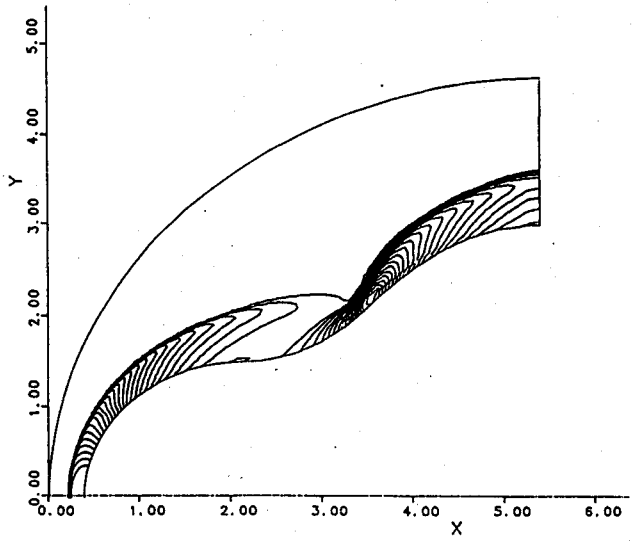

Fig. 6 Isobars for configuration 2 at freestream Mach number of 12.

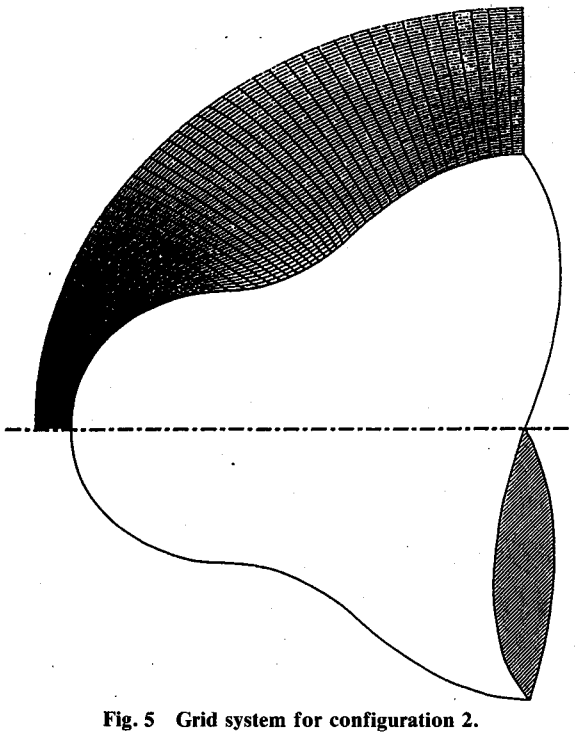

Fig. 5 Grid system for configuration 2.

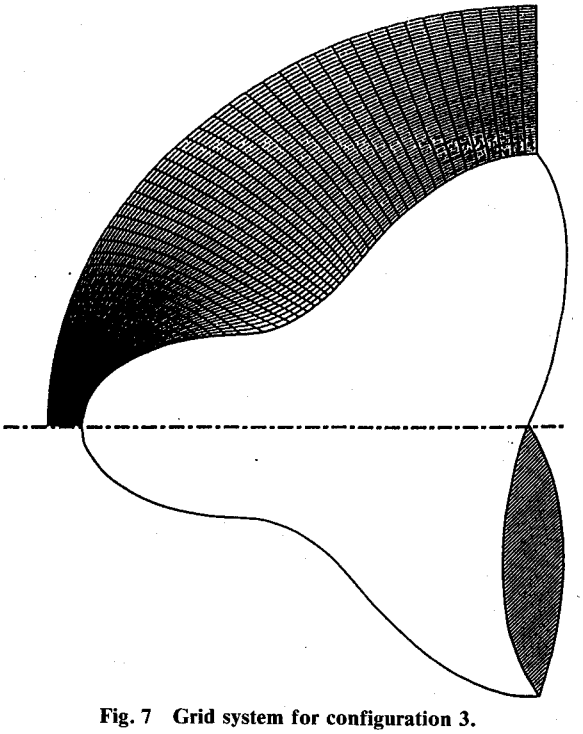

Fig. 7 Grid system for configuration 3.

hypersonic speeds and is illustrated in Fig. 5. The corresponding isobars for this configuration at Mach 12 are shown in Fig. 6 and can be compared directly with the unablated shape results from Fig. 3, also at Mach 12. Configuration 3 indicates a severe ablation case and is depicted in Fig. 7 along with the corresponding grid system. For this case the initial effective nose radius has also decreased dramatically, thereby altering the pressure distribution in the nosetip region. The pressure contours for this last configuration are shown in Fig. 8 for an increased Mach number of 18. Comparison with the unablated shape at Mach 18 from Fig. 4 illustrates significant changes in the bow-shock shape and interior shock-layer structure. The sequence of enhanced ablation from configuration 2 to 3 with a corresponding increase in freestream Mach number depicts a ground-launched hypervelocity projectile, which would ablate as it is accelerating. Conversely, re-entry vehicles would experience a decrease in Mach number while continuing to ablate with time.

The pressure contours for the indented geometries illustrate the complex expansion/compression process inside the computational domain, even for this inviscid flow model. As the

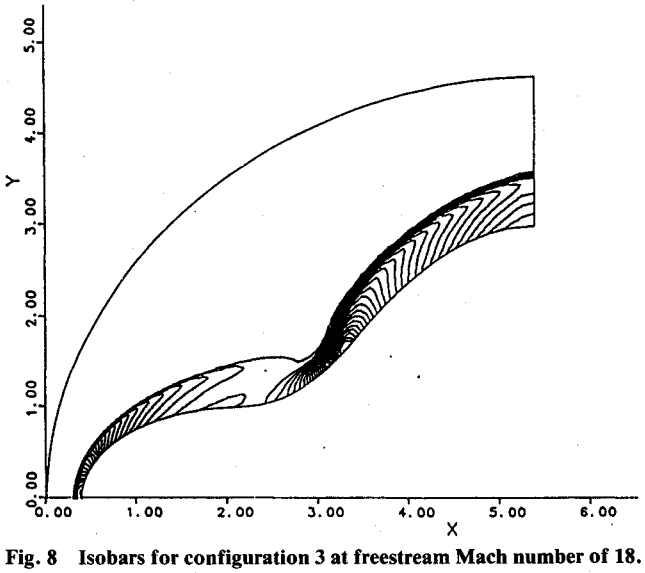

Fig. 8 Isobars for configuration 3 at freestream Mach number of 18.

flow moves away from the stagnation region, it expands to locally supersonic flow as it accelerates over the blunted nose cap. However, when the flow along the surface encounters a flare, compression waves are formed that coalesce into a shock wave. This process is clearly shown in Fig. 8. The pressure increase through this compression wave/shock wave structure is clearly sensitive to the geometry of the indentation and also the freestream Mach number. The flowfield behavior for a large indented shape is analogous to a Mach reflection type shock interaction with nonuniform freestream flow. If the change in slope of the concave section is very gradual, then flow recompression near the surface appears to be isentropic and the flare recovery pressure would be greatest. However, an abrupt change in surface slope of the concave section would produce a relatively strong recompression shock and, consequently, the recompression region would experience a lower recovery pressure on the flare. Figures 1-8 clearly demonstrate the ability of the numerical scheme to capture the shock/shock interactions and the expansion/compression regions within the computational domain.

A comparison of the nondimensionalized surface pressure at Mach 18 is illustrated in Fig. 9 for all three configurations. These data are plotted as a function of the distance along the axis of symmetry. Note the differences between configurations 2 and 3 in surface pressure. Also note the lower pressure for configuration 3 near the nosetip due to a smaller nose radius. One might suspect that the decreased configuration 3 pressure near the nose might offset some of the increase in drag coefficient due to higher pressure in the flare region. However, it is in fact the surface pressure distribution plotted vs the radial direction y (see Fig. 10) that indicates the relative differences in drag coefficient. Note that Fig. 10 clearly illustrates that a substantial increase in wave drag coefficient C_D would be associated with configuration 3. Also plotted in Fig. 10 are pressure distributions based on modified Newtonian theory. Note that the modified Newtonian theory works well near the nosetip but obviously fails to predict the strong shock-shock interaction region at the concave section. The drag coefficient is shown as a function of Mach number in Fig. 11 for configurations 1-3 along with comparison to modified Newtonian

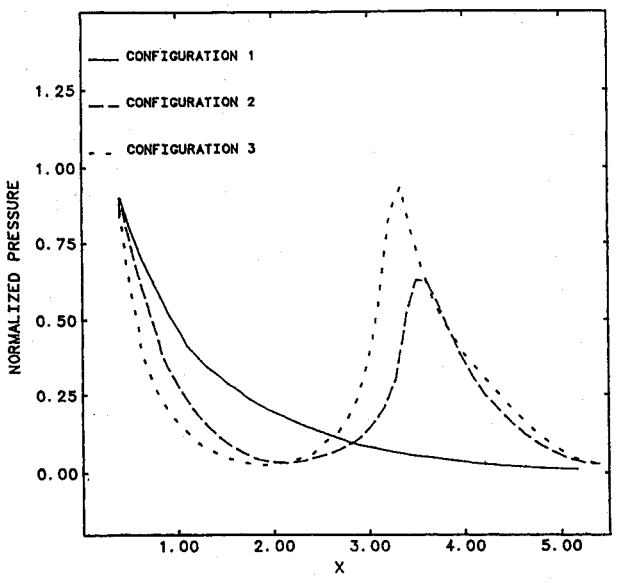

Fig. 9 Comparison of surface pressures along axis of symmetry for configurations 1-3 at freestream Mach number of 18.

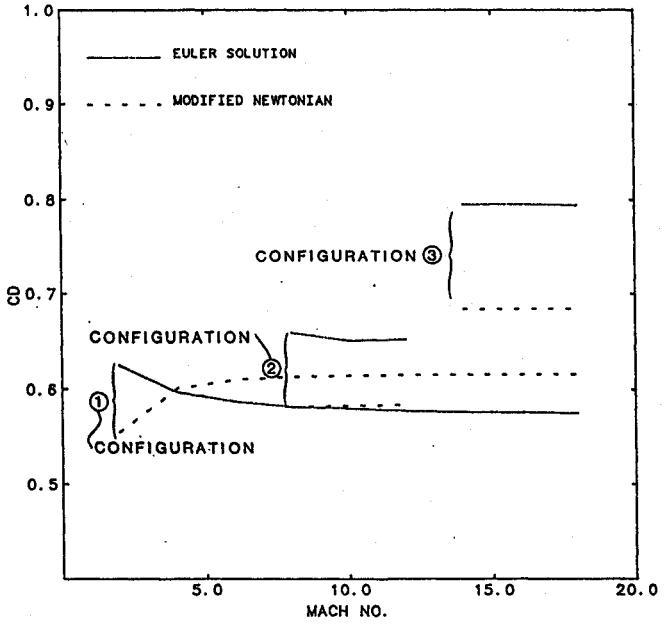

Fig. 11 Drag coefficient vs freestream Mach number for configurations 1-3.

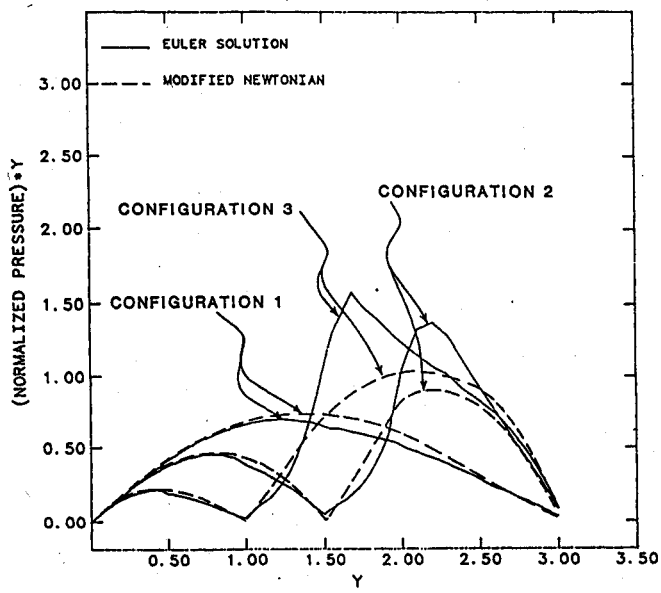

Fig. 10 Comparison of surface pressures along radial coordinate for configurations 1-3 at freestream Mach number of 18.

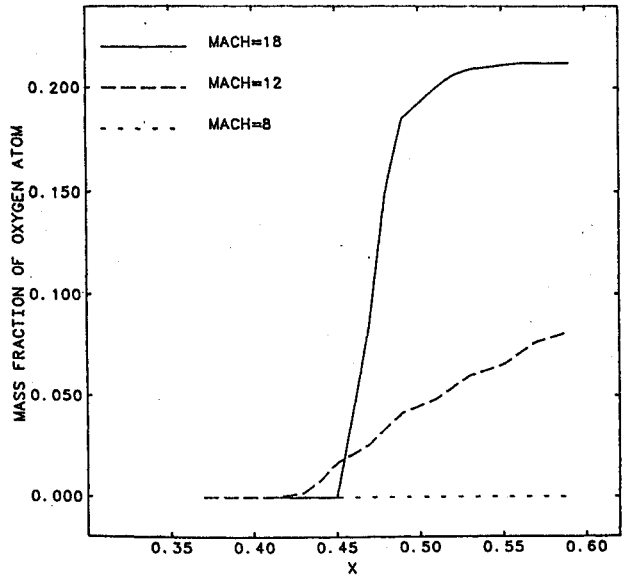

Fig. 12 Mass fraction of dissociated oxygen along stagnation streamline for configuration 1 at freestream Mach number of 18.

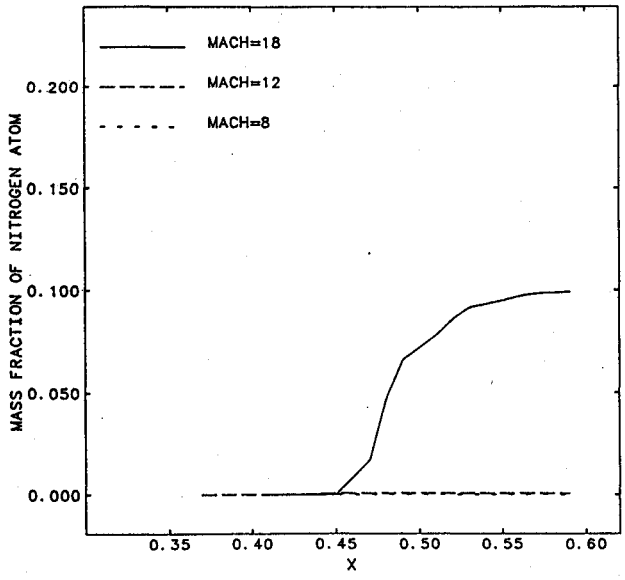

Fig. 13 Mass fraction of dissociated nitrogen along stagnation streamline for configuration 1 at freestream Mach number of 18.

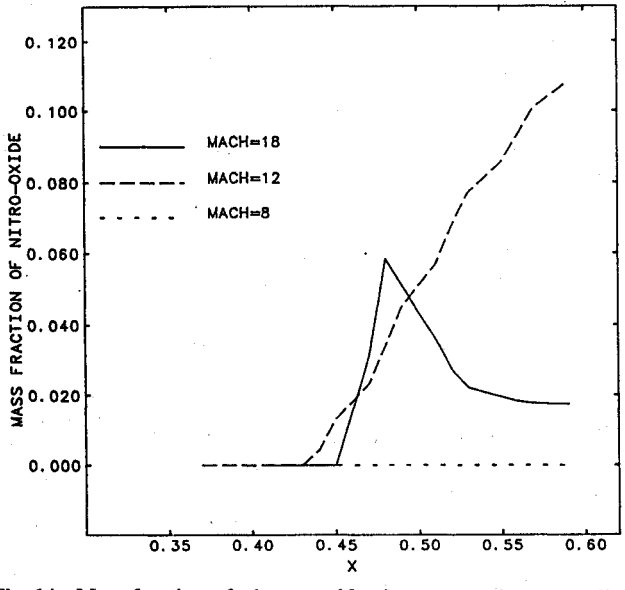

Fig. 14 Mass fraction of nitrous oxide along stagnation streamline for configuration 1 at freestream Mach number of 18.

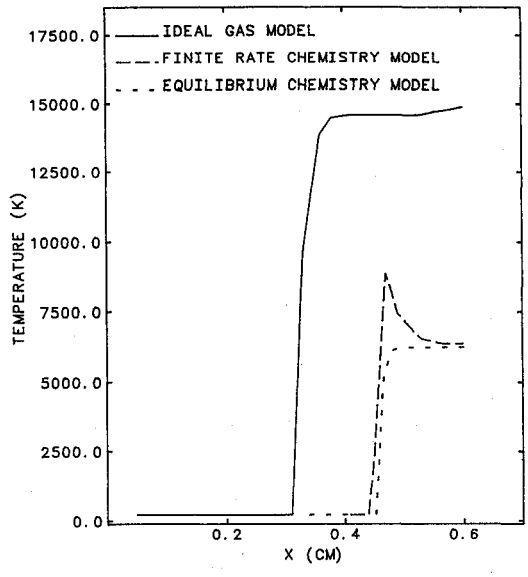

Fig. 15 Static temperature along stagnation streamline for configuration 1 at freestream Mach number of 18.

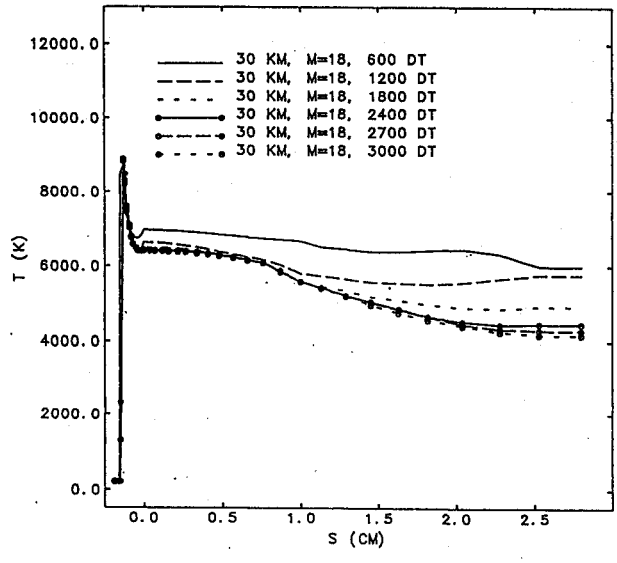

Fig. 16 Convergence history along the stagnation streamline.

theory. Of course, the drag curves shown in Fig. 11 illustrate only the wave drag and have been nondimensionalized by the base area of the vehicle. Note that modified Newtonian theory predicts the wrong trends altogether for the indented nose shapes. The action of viscosity in this problem would most likely produce a separation bubble at the beginning of the concave section, which would effectively reduce the wave drag contribution by decreasing the effective local slope of the inviscid surface streamlines.

The results discussed so far have not referenced the state of the chemical species in the flowfield. This omission is because the surface pressure is a function of the translational motion of the flowfield molecules and/or atoms and is somewhat insensitive to the chemical composition and equilibrium state of the gas. However, the reacting chemistry can have a direct affect on shock and standoff distance and shock structure. Also, the ability to calculate translational temperatures and chemical species mass fractions in nonequilibrium flows is important for future work in heat transfer and ablation studies. Therefore, nonequilibrium chemistry calculations have been included in the current analysis.

The mass species equations are solved using a scheme that decouples these equations from the gas dynamic equations. This technique, in which the gas dynamic variables at each iteration in time are determined first followed by the solution of the species equations, saves CPU time and computer memory over more conventional coupled schemes. However, the decoupled approach has its own disadvantages, namely, determination of an appropriate chemistry time step relative to the gas dynamics time step. A stability analysis of the implicit solution to the chemical equations has established some guidelines for the size of the chemical time step based on freestream conditions and geometry (i.e., whether flow is likely to be in chemical equilibrium or not). For the current investigation at low-altitude conditions, the chemical time step was typically one order of magnitude smaller than the comparable gas dynamic time step.

A comparison of the amount of chemical reactions along the stagnation streamline ahead of the body is presented in the form of mass fractions in Figs. 12–14 for Mach numbers of 8, 12, and 18. Figure 12 shows the growth in monotomic oxygen as the Mach number (and dissociation) increases. The internal energy levels required for the dissociation of diatomic nitrogen are much higher than those for oxygen as illustrated in Fig. 13.

Also a byproduct of dissociating oxygen and nitrogen is the formation of NO as presented in Fig. 14. The general qualitative trend in Figs. 12–14 is that the amount of chemical activity is proportional to the freestream kinetic energy (i.e., Mach number) and is too significant to ignore for large hypersonic Mach numbers. Finally, the result of chemical dissociation is to lower the thermal energy levels (i.e., static temperature) from that modeled by a calorically perfect gas. This trend is illustrated for configuration 1 at Mach 18 along the stagnation line ahead of the nosetip in Fig. 15. Note that in this figure the temperature of the air is about half of that predicted using a nonreacting gas (i.e., ideal gas). This figure also includes computations using an equilibrium model.[18] The peak in the temperature distribution in Fig. 15 indicates a region within the domain where the flow is in a nonequilibrium state. Furthermore, it is observed that an equilibrium state is achieved near the body surface. Because of the higher density ratios across a shock associated with chemically reacting flows, the shock standoff distance is dramatically reduced from that of an ideal gas. Also note that the physical scale of the geometry does not affect the Euler equation results but can have a dramatic affect on the nonequilibrium nature of the chemical reactions. Finally, Fig. 16 indicates the solution convergence history along the stagnation streamline. The stagnation point is set at $S = 0$, and positive values of S indicate the distance along the body surface. Note that the solution converges within 1200 time steps (iterations) near the nose region, whereas it takes about 3000 time steps to converge downstream. This discrepancy in convergence rates is most likely caused by grid point distribution. As mentioned previously, very dense clustering was enforced in the vicinity of the stagnation region leaving a somewhat coarser grid on the aft section of the body.

Conclusions

The use of CFD techniques has been demonstrated for complex nose shapes involving strong shock/shock interactions and compression/expansion regions. Calculations of surface pressures and wave drag coefficients have been presented for indented blunt bodies over a wide range of Mach numbers. The effect of a chemically dissociating flowfield has also been illustrated. This numerical approach will serve as an important precursor step to more meaningful viscous and heat transfer computations in hypersonic chemically reacting flowfields.

References

[1]Stetson, K. F., "Hypersonic Boundary Layer Transition Experiments," Flight Dynamics Lab., Air Force Wright Astronautical Lab., Wright-Patterson AFB, OH, AFWAL-TR-80-3062, Oct. 1980.

[2]Hoffmann, K. A., Wilson, D. E., and Hamburger, C., "Aerothermodynamic Analysis of Projectiles at Hypersonic Speeds," *Proceedings of AIAA 7th Applied Aerodynamics Conference*, July 1989.

[3]Holden, M. S., "A Review of Aerothermal Problems Associated with Hypersonic Flight," AIAA Paper 86-0267, Jan. 1986.

[4]Ingram, M. W., Wilson, D. E., Hoffmann, K. A., and Pratup, S. B., "Electric Gun Technology Assessment," Center for Electromechanics, Univ. of Texas at Austin, Austin, TX, Final Rept. RF-68, 1987.

[5]Steger, J. L., "Implicit Finite-Difference Simulation of Flow About Arbitrary Two-Dimensional Geometries," *AIAA Journal*, Vol. 16, No. 7, 1978, pp. 679–686.

[6]Blottner, F. G., and Larson, D. E., "Navier-Stokes Code NS3D for Blunt Bodies, Part I: Analysis, Results, and Verification," Sandia National Lab., Albuquerque, NM, SAND88-0504/1, 1988.

[7]Roe, P. L., "Approximate Riemann Solvers, Parameter Vectors, and Difference Schemes," *Journal of Computational Physics,* Vol. 43, 1981, pp. 357–372.

[8]Van Leer, B., "Flux-Vector Splitting for the Euler Equations," *Lecture Notes in Physics,* Vol. 170, Springer, Berlin, 1982, pp. 507–512.

[9]Palmer, G., "An Implicit Flux-Split Algorithm to Calculate Hypersonic Flowfields in Chemical Equilibrium," AIAA Paper 87-1580, 1987.

[10]Steger, J. L., and Warming, R. F., "Flux Vector Splitting of the Inviscid Gas Dynamics Equations with Application to Finite Difference Methods," NASA TM-78605, July 1979.

[11]Hoffmann, K. A., "Computational Fluid Dynamics for Engineers," EES, Austin, TX, 1989.

[12]Beam, R. M., and Warming, R. F., "An Implicit Factored Scheme for the Compressible Navier-Stokes Equations," *AIAA Journal*, Vol. 16, No. 5, 1978, pp. 393–402.

[13]"MACSYMA Reference Manual – Version 10," Mathlab Group, Lab. for Computer Science, Massachusetts Inst. of Technology, Cambridge, MA, Jan. 1983.

[14]Thompson, J. F., Thames, F. C., and Mastin, C.W., "Boundary-Fitted Curvilinear Coordinate Systems for Solution of Partial Differential Equations on Fields Containing Any Number of Arbitrary Two-Dimensional Bodies," NASA CR-2729, July 1977.

[15]Lee, J.-H., "Basic Governing Equations of the Flight Regimes of Aeroassisted Orbital Transfer Vehicles," *Progress in Astronautics and Aeronautics: Thermal Design of Aeroassisted Orbital Transfer Vehicles*, Vol. 96, edited by H. F. Nelson, AIAA, New York, 1985.

[16]Park, C., "Convergence of Computation of Chemically Reacting Flows," AIAA Paper 85-0247, 1985.

[17]Chiang, T. L., and Hoffmann, K. A., "Determination of Computational Time Step for Chemically Reacting Flows," AIAA Paper 89-1855, June 1989.

[18]Tannehill, J. C., and Mugee, P. H., "Improved Curve Fits for Thermodynamic Properties of Equilibrium Air Suitable for Numerical Computation Using Time-Dependent or Shock-Capturing Methods," NASA CR-2470, Oct. 1974.

Walter B. Sturek
Associate Editor